Journal of Materials Chemistry B

ROYAL SOCIETY OF CHEMISTRY

PAPER

View Article Online
View Journal | View Issue

Cite this: J. Mater. Chem. B, 2025, 13, 3730

Dual-responsive polydopamine-embellished Zn-MOFs enabling synergistic photothermal and antibacterial metal ion therapy for oral biofilm eradication†

Ge Pan,[ab] Jinyao Zheng,[c] Zongjia Li,[c] Qian Duan, *[a] Miaomiao Zhang*[b] and Dapeng Wang *[b]

Received 29th October 2024,
Accepted 10th February 2025

DOI: 10.1039/d4tb02427c

rsc.li/materials-b

Oral biofilms are associated with various oral diseases causing pain and discomfort, and pose a severe threat to general health. Conventional surgical debridement and antibacterial therapy often yield unsatisfactory outcomes because they either fail to fully and painlessly eliminate biofilms or increase the risk of bacterial resistance. In this study, we synthesized polydopamine-embellished Zn-MOFs (ZIF-8@PDA NPs), which can degrade under mildly acidic conditions to release Zn^{2+}. These nanoparticles also convert near-infrared light energy into heat, thereby enabling synergistic photothermal and antibacterial metal ion therapy for oral biofilm eradication. Our findings reveal that therapy with ZIF-8@PDA NPs, when exposed to near-infrared radiation, demonstrates exceptional antibacterial efficacy and is highly effective in eradicating oral biofilms both *in vitro* and *ex vivo*. Furthermore, we used an *in vivo* rodent tooth biofilm model to demonstrate the suppression of dental caries. This work presents a promising solution for preventing and suppressing dental caries as well as other treating diseases linked to oral biofilm infections.

1. Introduction

The microbiomes residing within the human oral cavity are the second most abundant in the body.[1,2] Insufficient oral hygiene, improper use of antibiotics, lifestyle factors (such as smoking), and alterations in saliva can precipitate dysbiosis of the oral microbiota, which is primarily composed of bacteria.[3] This dysbiosis could culminate in the formation of a sophisticated and intricately organized assemblage known as the oral biofilm.[4] Oral biofilms are associated with various oral diseases, including caries, periodontal disease, pulpitis, and candidiasis, which can cause pain and discomfort, and in severe cases, may lead to tooth loss or systemic health complications.[1,5] Extracellular polymeric substances (EPSs) are complex mixtures of biopolymers produced by microorganisms within biofilms.[5] The adhesion and protective effects of EPSs in microbial biofilms render innate immune cells and conventional antimicrobials inefficient in degrading oral biofilms and eradicating embedded microbes.[6] In addition, pathogenic bacteria can ferment sugars from food sources. During this process, they metabolize sugars and produce acids as metabolic byproducts in the oral cavity.[7] These acids can lower the pH levels in the immediate environment surrounding the bacteria, culminating in the onset of dental caries and other oral pathologies.[5] Therefore, eradicating oral biofilms holds considerable significance for the prevention and treatment of oral biofilm-related diseases.

The primary clinical treatments for oral biofilm infections currently involve mechanical debridement and antibiotic therapy.[8] However, these methods have certain limitations. Surgical debridement, while effective in removing biofilms and diseased tissues, can lead to discomfort, pain, and potential complications such as bleeding or adverse reactions to anesthesia.[9] Although antibiotic therapy has greatly improved treatment comfort, its overuse or inappropriate use can contribute to the development of drug resistance in oral pathogenic bacterial strains, making infections more difficult and costly to treat.[10,11] Therefore, there is an urgent need to explore novel antibacterial strategies to effectively eradicate oral biofilms and prevent their recolonization. At present, novel antimicrobial strategies have been continuously developed,[12] such as controlled release of antibiotics,[13] polypeptides,[14] nanoparticles,[15–18] antibacterial metal ions,[19,20] metal–organic frameworks,[21,22] polymers,[23] bacteriophages,[24] antibacterial lysozymes,[25] *etc.* Many promising

[a] School of Materials Science and Engineering, Changchun University of Science and Technology, Changchun, 130022, P. R. China. E-mail: duanqian88@hotmail.com
[b] State Key Laboratory of Polymer Physics and Chemistry, Changchun Institute of Applied Chemistry Chinese Academy of Sciences, Changchun, 130022, P. R. China. E-mail: wdp@ciac.ac.cn, mmzhang@ciac.ac.cn
[c] State Key Laboratory of Electroanalytical Chemistry, Changchun Institute of Applied Chemistry, Chinese Academy of Sciences, Changchun, 130022, P. R. China

† Electronic supplementary information (ESI) available. See DOI: https://doi.org/10.1039/d4tb02427c

antibacterial therapy strategies based on nanoparticles have been developed,[7] including photothermal therapy (PTT),[26,27] photodynamic therapy (PDT),[28–30] chemodynamic therapy (CDT),[31–33] and so on. Every solution has its own unique advantages and limitations. For example, PTT exploits photothermal agents to convert light energy into heat, inducing local hyperthermia. This approach not only effectively kills bacteria but also achieves excellent non-mechanical removal of oral biofilms, making it a promising option for biofilm eradication.[34–36] Although promising, PTT faces challenges in regulating the treatment temperature, as excessively high temperatures can damage surrounding tissues, while insufficient heat may result in incomplete bacterial ablation.[37] Synergistic strategies have been proposed to tackle this issue, such as the integration of PTT with CDT or, PDT,[27,34,38] immunotherapy,[39,40] and so on.[8,31,34,41,42] Nevertheless, applying PTT in oral biofilm therapy still faces two notable concerns: short action duration and limited permeability.[43,44] These concerns could be addressed by synergistically combining bactericidal metal ions that are released on demand. Metal ions, such as zinc ions (Zn^{2+}), exhibit broad-spectrum antibacterial activity by interfering with the metabolic process of infected bacteria.[45] Zinc metal–organic frameworks (Zn-MOFs), composed of Zn^{2+} connected by multidentate organic linkers, can be regarded as ideal reservoirs of Zn^{2+} because Zn-MOFs could dissociate to release Zn^{2+} *via* hydrolysis-induced decomposition when exposed to acidic conditions.[46] Given their ability to release Zn^{2+} in response to pH changes, Zn-MOFs are expected to enhance PTT for antibacterial therapy and biofilm eradication, which are typically acidic due to bacterial metabolism.

In this work, zinc imidazolate framework-8 (ZIF-8) was chosen as the Zn^{2+} reservoir from various Zn-MOFs due to its simple synthesis procedure and pH-responsive characteristics, allowing it to release Zn^{2+} in the acidic environment of oral biofilms. The surface of ZIF-8 was coated with polydopamine (PDA) to prepare polydopamine-embellished Zn-MOFs (ZIF-8@PDA NPs), as shown in Fig. 1a. In our design, the PDA coating on the surface of ZIF-8 NPs not only facilitated the effective adhesion of ZIF-8@PDA NPs to the bacterial biofilm surface, but also endowed them with significant photothermal properties. Under 808 nm near-infrared (NIR) irradiation, ZIF-8@PDA NPs efficiently converted NIR light into heat, inducing local hyperthermia. Simultaneously, ZIF-8@PDA NPs gradually degraded in the mildly acidic microenvironment, releasing a significant amount of Zn^{2+} ions. These ions could penetrate the

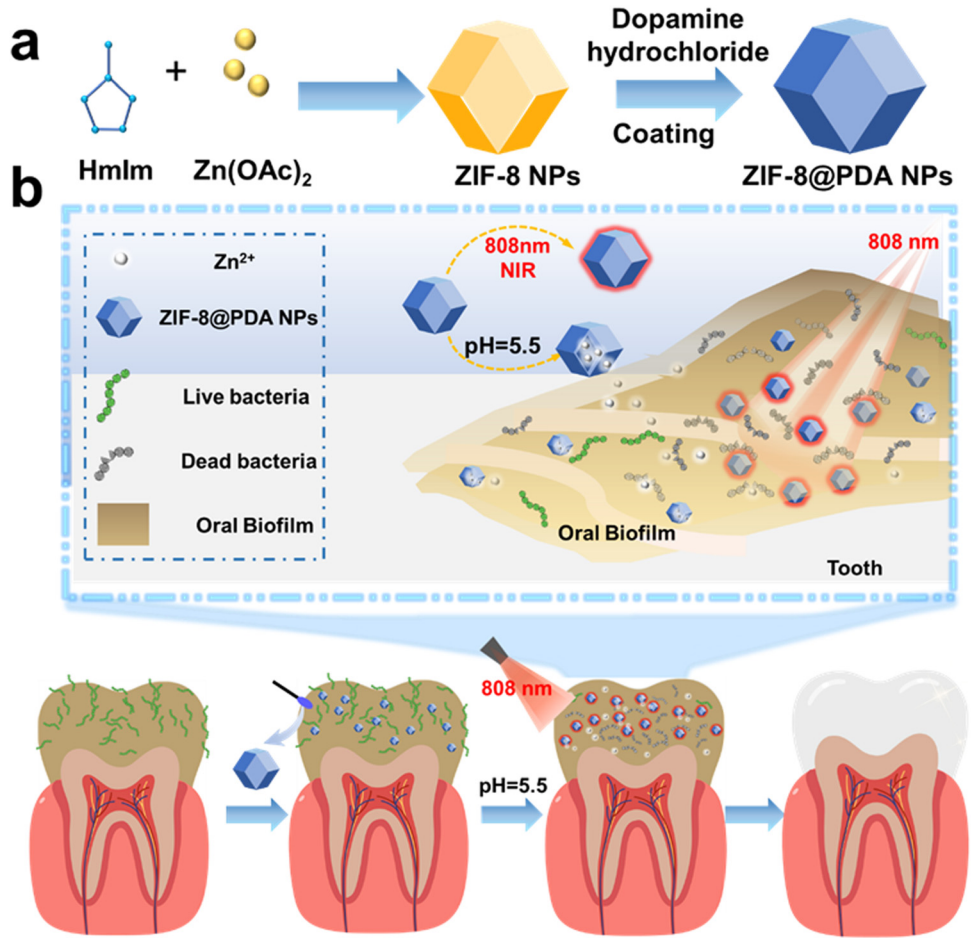

Fig. 1 (a) Schematic illustration of the preparation process of ZIF-8@PDA NPs. (b) Schematic representation of the ZIF-8@PDA NPs synergizing photothermal and antibacterial metal ion therapy for oral biofilm eradication.

inner layers of the biofilm, effectively eradicating *S. mutans* and disrupting the biofilm they formed through a synergistic combination of photothermal effects and antibacterial metal ions (Fig. 1b). In addition, we established an *ex vivo* tooth infection model and an *in vivo* dental caries mouse model to study the effectiveness of ZIF-8@PDA NPs in removing oral biofilms.

2. Results and discussion

2.1. Preparation and characterization of ZIF-8@PDA NPs

ZIF-8@PDA NPs can be easily synthesized under mild conditions, as shown in Fig. 1a. Firstly, zinc acetate dihydrate ($Zn(OAc)_2{\cdot}2H_2O$) and 2-methylimidazole (HmIm) were used to produce ZIF-8 NPs. Then, a PDA coating was naturally deposited onto the surface of ZIF-8 to form ZIF-8@PDA NPs. Our findings demonstrate a progressive enhancement in the photothermal effect of ZIF-8@PDA NPs with increasing PDA content (Fig. S1a, ESI†), however, this enhancement is accompanied by the potential for elevated temperature-induced thermal damage to tissues. Concurrently, the increase in the PDA proportion markedly decelerates the degradation rate of the material, resulting in a significant reduction in Zn^{2+} release (Fig. S1b, ESI†). To achieve an optimal balance between photothermal performance and Zn^{2+} release efficiency, an optimal ZIF-8 to PDA ratio of 5 : 2 was ultimately established.

The morphology of ZIF-8 NPs is characterized as a polyhedral structure with an average diameter of 440 nm, as illustrated in Fig. 2a–c. Zeta potential measurements indicated that the potential of ZIF-8 decreased from 9.6 mV to −0.3 mV after coating with PDA (Fig. 2d), attributable to the negative charge of PDA. The PDA coating has scarcely altered the morphology of ZIF-8 (Fig. 2e and f). Upon PDA coating, the diameter of resulting ZIF-8@PDA NPs is increased to 460 nm, suggesting that the thickness of the PDA coating is approximately 10 nm (Fig. 2h). The energy spectrum showed uniform distributions of the four elements: carbon (C), nitrogen (N), zinc (Zn), and oxygen (O) in

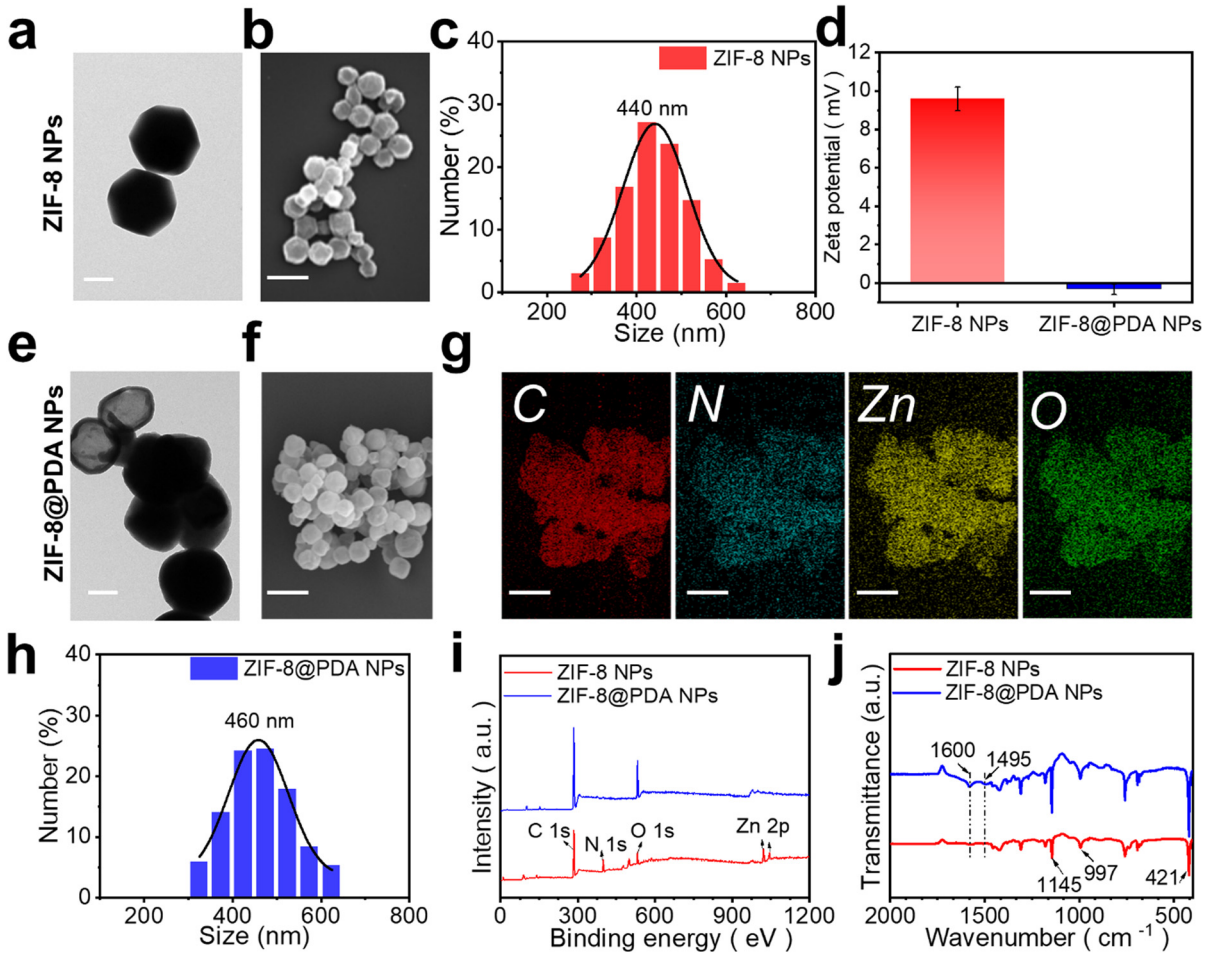

Fig. 2 Characterization of ZIF-8 NPs and ZIF-8@PDA NPs. (a) TEM image, (b) SEM image, and (c) particle size distribution of ZIF-8 NPs. Scale bars in the TEM and SEM images are 200 nm and 1000 nm, respectively. (d) Zeta potential of ZIF-8 NPs and ZIF-8@PDA NPs. (e) TEM image and (f) SEM image of ZIF-8@PDA NPs, with (g) the corresponding EDS mapping displaying C, N, Zn, and O within the ZIF-8@PDA NPs. The scale bars in the TEM and SEM images are 200 and 1000 nm, respectively. (h) Particle size distribution of ZIF-8@PDA NPs. (i) XPS results and (j) FTIR spectra of ZIF-8 NPs and ZIF-8@PDA NPs. For clarity, the results of ZIF-8 NPs have been shifted downwards. Data are presented as mean ± standard deviation with n = 3.

ZIF-8@PDA NPs (Fig. 2g). Fig. 2i shows the XPS patterns of ZIF-8 NPs and ZIF-8@PDA NPs. Comparatively, we observed that two binding energy peaks appeared at 1021 and 1045 eV for ZIF-8 NPs, which can be attributed to the Zn $2p_{3/2}$ and Zn $2p_{1/2}$ orbitals (Fig. S2a, ESI†).[47,48] In contrast, these peaks are absent for the ZIF-8@PDA NPs. This phenomenon has been previously observed and can be ascribed to the chelation of the catechol moiety of DA with the Zn^{2+} metal nodes.[49] This is because the Zn 2p spectra are associated with the oxidation state of zinc, leading to the disruption of the Zn–Mim coordination bonds in the parent ZIF-8 NPs.[49] The peaks emerged at 399.1 eV, 284.8 eV, and 533.0 eV in the XPS spectra of ZIF-8@PDA NPs correspond to N 1s, C 1s, and O 1s, respectively.[50] Note that the X-ray diffraction pattern of ZIF-8@PDA NPs is identical to that of ZIF-8 NPs (Fig. S2b, ESI†), indicating that the PDA coating almost has not altered the crystal structure of ZIF-8 NPs.[51] Moreover, the ultraviolet-visible (UV-vis) spectra provide evidence for the successful coating of polydopamine (PDA) on ZIF-8 NPs, as illustrated in Fig. S2c (ESI†). The FTIR spectrum of ZIF-8@PDA NPs reveals peaks at 1495 and 1600 cm^{-1} that were assigned to the benzene skeleton vibrations of PDA (Fig. 2j).[52] Combined with the peak at 421 cm^{-1} corresponding to the Zn–N bond and the peaks at 1145 and 997 cm^{-1} corresponding to the C–N bond, FTIR results further confirmed the successful coating of PDA on ZIF-8 NPs. Taken together, all results confirmed the successful synthesis of ZIF-8@PDA NPs. Simultaneously, as the control group of the photothermal experiment, we synthesized PDA NPs, and the results presented in Fig. S3a and b (ESI†) indicate that their diameter is 250 nm.

2.2. pH responsiveness and photothermal effect of ZIF-8@PDA NPs

As mentioned in the introduction, pathogenic bacteria are capable of metabolizing sugars, thereby lowering pH in the oral microenvironment by producing acidic metabolic by-products. This acidic environment can lead to the demineralization of the tooth's hard tissue, contributing to the formation of caries' lesions. Conversely, the acidic conditions can also be leveraged as a stimulus to perform controlled antibacterial actions. Note that the framework structure of ZIF-8 could be disrupted in an acidic environment, leading to the release of the Zn^{2+} ions contained within.[21] To evaluate the pH responsiveness of ZIF-8@PDA NPs, they were suspended in PBS solutions of varying pH for 2 h, and their morphology was examined *via* SEM (Fig. 3a). As the pH declined, the three-dimensional framework of ZIF-8@PDA NPs gradually disintegrated. When suspended in a solution at a pH of 5.5 for 2 h, some ZIF-8@PDA NPs were nearly entirely dissociated. To quantitatively evaluate the dissociation rate of ZIF-8@PDA NPs, the NPs were suspended in PBS solutions with different pH levels for

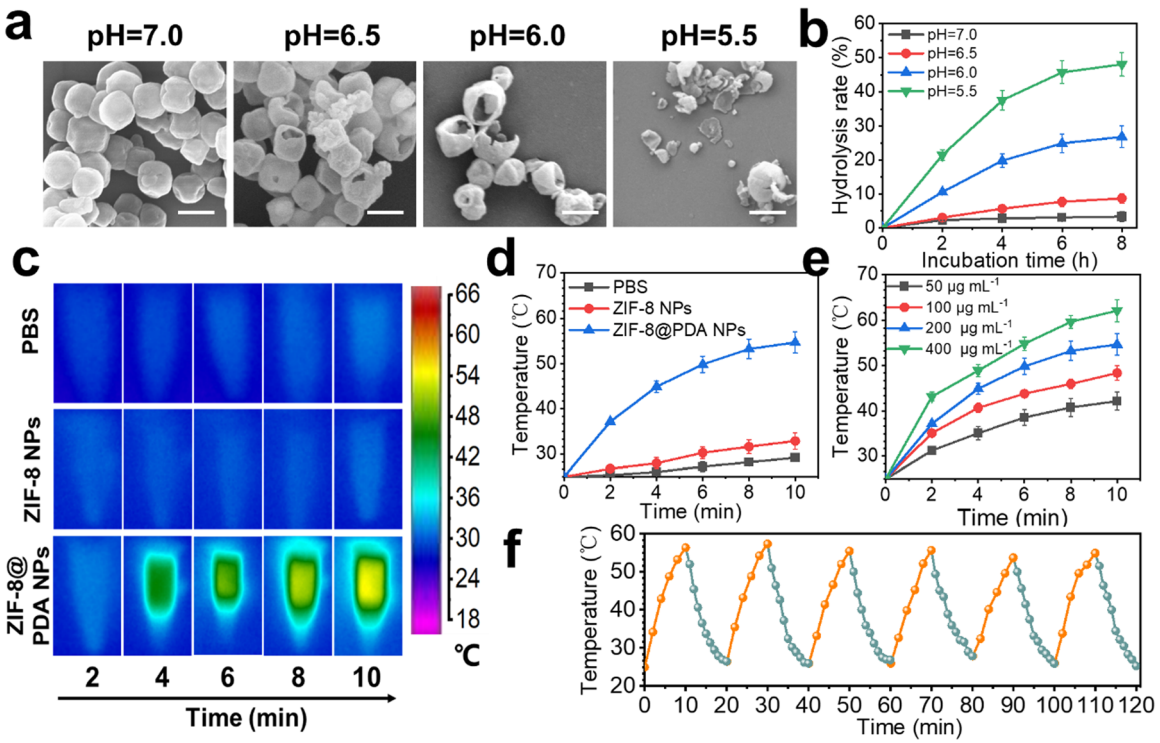

Fig. 3 pH responsiveness and photothermal effect of ZIF-8@PDA NPs. (a) SEM images of ZIF-8@PDA NPs in solutions of varying pH after 2 h. The scale bar represents 500 nm. (b) Hydrolysis rate of ZIF-8@PDA NPs in solutions of different pH over different durations. (c) Infrared thermal photographs of PBS solution and solutions containing ZIF-8 NPs and ZIF-8@PDA NPs under 808 nm laser (1.5 W cm^{-2}, 10 min). (d) Temperature *versus* time curves for PBS solution and solutions containing ZIF-8 NPs and ZIF-8@PDA NPs under an 808 nm laser (1.5 W cm^{-2}, 10 min). (e) Temperature *versus* time curves for solutions containing ZIF-8@PDA NPs of different concentrations under an 808 nm laser (1.5 W cm^{-2}). (f) Temperature variations of ZIF-8@PDA NP solution at six rounds of alternating NIR laser activation and deactivation. Data are presented as mean ± standard deviation with n = 3.

durations of 2, 4, 6, and 8 h. We employed centrifugation to isolate undegraded ZIF-8@PDA NPs, with the residual quantity ascertained through precise weighing. Fig. 3b illustrates the hydrolysis rate of ZIF-8@PDA NPs under different pH conditions and durations. Generally, extending the duration can enhance the hydrolysis rate. When the solution pH reaches 5.5, an 8-hour immersion results in a hydrolysis rate of 48 ± 3.5%. These results corroborated that in an acidic environment, the ZIF-8@PDA NPs can gradually disassociate, with a faster hydrolysis rate observed as the pH value decreases.

Next, we investigated the photothermal conversion performance of ZIF-8@PDA NPs under NIR irradiation. For the NIR source, we employed an 808 nm laser operating at a power density of 1.5 W cm^{-2}. The ZIF-8 NPs, PDA NPs, and ZIF-8@PDA NPs were suspended in PBS solutions. As a control, we observed that the NIR irradiation caused only a marginal increase in temperature for either the PBS solution or ZIF-8 NP solution (Fig. 3c and d). In contrast, the temperature of ZIF-8@PDA NP solutions showed a noticeable increase after 10 min laser irradiation, highlighting their noticeable photothermal conversion performance (Fig. 3c and d). The temperature increase depended on the concentration of ZIF-8@PDA NPs (Fig. 3e). Furthermore, we studied the photothermal stability of ZIF-8@PDA NPs by alternately activating and deactivating the NIR laser at ten-minute intervals. After six alternating cycles, the photothermal effect of the ZIF-8@PDA NP solution did not change. It remained consistently at 55 ± 2 °C (Fig. 3f) and the photothermal conversion efficiency of ZIF-8@PDA NPs was 37%, indicating the good photothermal stability of the ZIF-8@PDA NPs. The photothermal effect is known to kill bacteria *via* local hyperthermia and oxidative stress induction in some cases.[53] The maximum temperature of 55 °C is considered safe for the oral mucosa, making it suitable for application in the oral environment.[34] The measurements of photothermal conversion and Zn^{2+} release of ZIF-8@PDA NPs could serve as a foundation for evaluating their antibacterial properties and effectiveness in eradicating oral biofilms *in vitro*, *ex vivo*, and *in vivo*.

2.3. Antibacterial efficacy *in vitro*

The antibacterial efficacy of ZIF-8@PDA NPs was assessed using the representative oral pathogenic bacteria, *Streptococcus mutans* (*S. mutans*). Fig. 4a shows *S. mutans* (1×10^6 CFU mL^{-1}) that were treated with (I) PBS solution (control), (II) $Zn(OAc)_2{\cdot}2H_2O$ solution at 20 μg mL^{-1}, (III) ZIF-8 NPs solution at 200 μg mL^{-1}, (IV) PDA NP solution at 200 μg mL^{-1} under an 808 nm laser (1.5 W cm^{-2}, 10 min), (V) ZIF-8@PDA NP solution at 200 μg mL^{-1} and (VI) ZIF-8@PDA NPs solution at 200 μg mL^{-1} under an 808 nm laser (1.5 W cm^{-2}, 10 min), respectively for 6 h at 37 °C. Fig. 4b shows representative photographs of the colonies formed on agar plates after various treatments. We found that Zn^{2+} from $Zn(OAc)_2{\cdot}2H_2O$ and ZIF-8 NPs exhibited certain antibacterial properties. The photothermal effect can also produce a significant antibactericidal effect as evidenced by the results obtained using PDA NPs with NIR light. Notably, after being irradiated with NIR light, the CFU of the bacteria incubated with ZIF-8@PDA NPs showed a 5-log reduction (Fig. 4d). A comparative analysis of the results with and without NIR irradiation highlighted the synergistic action of photothermal and Zn^{2+} in eliminating *S. mutans*. Furthermore, bacterial morphology was examined using SEM, revealing the most significant membrane contraction in the ZIF-8@PDA + NIR group (Fig. 4c). Additionally, the residual shell of ZIF-8@PDA NPs adhering to the surface of bacteria was also observed. This suggested that the ZIF-8@PDA NPs function by initially adhering to the bacterial surface and subsequently inducing a photothermal effect combined with Zn^{2+} to kill the bacteria.

Pathogenic bacteria can ferment sugars from food sources to produce acids, leading to a decrease in pH below 5.5.[54] To study whether the presence of pathogenic bacteria can lower the environmental pH, we examined the pH values of the bacterial solution. As shown in Fig. 4e, the pH values of *S. mutans* suspensions steadily decreased and ultimately reached approximately 5.0 after 6 h in the presence of 1% sucrose. These measurements demonstrated the acid-producing ability of *S. mutans*. Interestingly, the pH values of the bacterial suspensions remain approximately constant when co-cultured with ZIF-8@PDA NPs and subjected to NIR irradiation (Fig. 4e). In addition, the bacteria were co-cultured with ZIF-8@PDA NPs at different pH values, and the OD values at 600 nm (OD_{600nm}) were recorded, as this measurement is commonly used to monitor bacterial viability.[55] Fig. 4f shows that after coculturing with ZIF-8@PDA NPs, the OD values of the oral bacteria changed; lower pH values under the culture conditions resulted in greater changes in OD_{600nm}. This indicated that the antibacterial capability of ZIF-8@PDA NPs increases with decreasing pH value. This could be attributed to the release of Zn^{2+}.[46] Taken together, these experiments demonstrated that ZIF-8@PDA NPs can respond to the weakly acidic environment of oral bacterial biofilms, making them more effective at killing bacteria at lower pH values.

2.4. Efficacy of ZIF-8@PDA NPs for oral biofilm eradication *in vitro*

We further evaluated whether ZIF-8@PDA NPs could effectively eradicate oral biofilms, which were formed by *S. mutans* and 1% sucrose in BHI at 37 °C for 24 h. As illustrated in Fig. 5a, the established biofilms underwent five various treatments. The live/dead BacLight bacterial viability kit was used to evaluate and assess bacterial viability, where dead or dying bacteria cells with damaged membranes were stained red, while live bacteria cells with intact membranes were stained green.[56] The 3D reconstructed confocal images revealed that in the control group, where no NPs were added, green fluorescence was evenly distributed, and virtually no red fluorescence was observed (Fig. 5b). This signified a high concentration of live bacteria within the biofilm. After treatment with Zn^{2+} and ZIF-8 NPs, a significant amount of green fluorescence was still observed, indicating the presence of abundant viable bacteria within the biofilm. Notably, a significant reduction in green fluorescence and a marked decrease in biofilm thickness were observed when ZIF-8@PDA NPs were used in conjunction with NIR (Fig. 5b and c), indicating that ZIF-8@PDA NPs could effectively

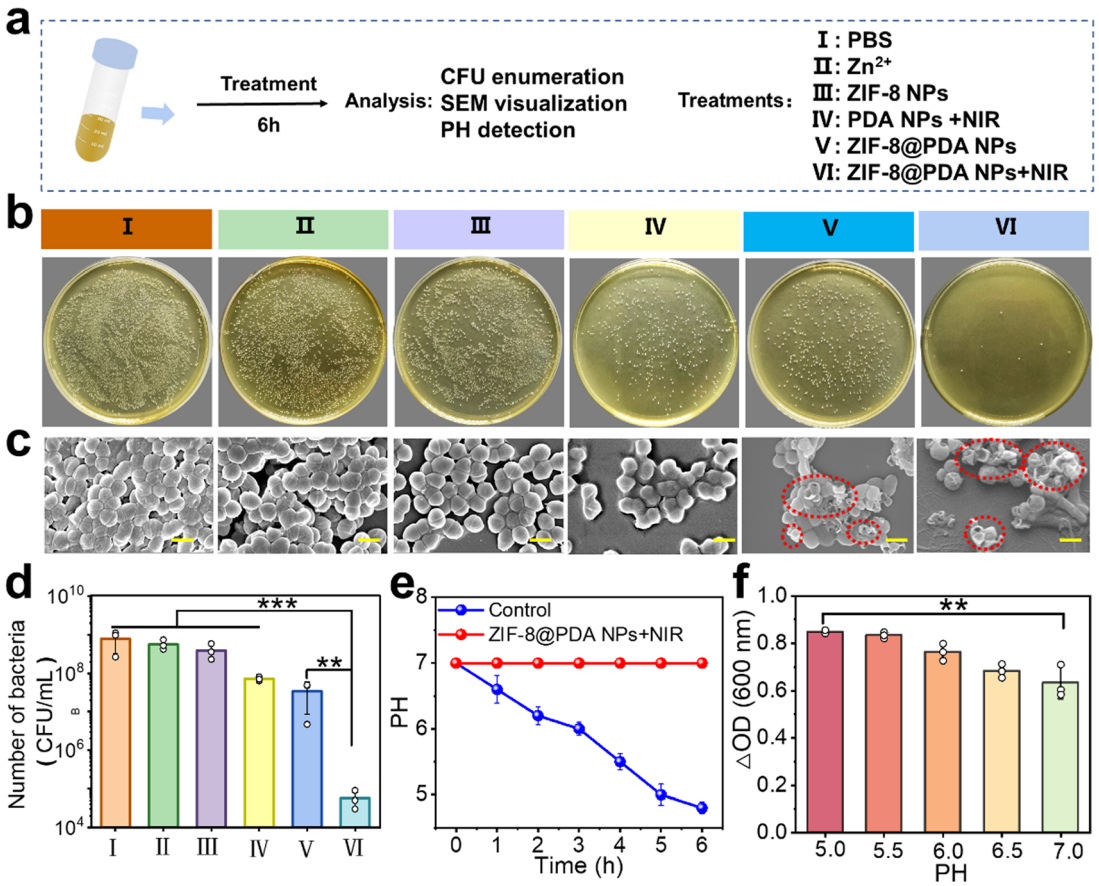

Fig. 4 Antibacterial activity *in vitro*. (a) Illustration of the antibacterial experiments of *S. mutans* with different treatments: (I) the control (PBS solution), (II) $Zn(OAc)_2{\cdot}2H_2O$ solution, (III) ZIF-8 NP solution, (IV) PDA NP solution under an 808 nm laser, (V) ZIF-8@PDA NP solution and (VI) ZIF-8@PDA NP solution under an 808 nm laser (b) Representative photographs of *S. mutans* colonies formed on the BHI agar plates after different treatments. (c) Representative SEM images and (d) CFU enumeration of *S. mutans* after different treatments. The scale bar represents 1 μm. (e) Time-dependent changes in pH for the *S. mutans* suspension and the *S. mutans* suspension co-cultured with ZIF-8@PDA NPs. (f) Changes in OD_{600nm} of the *S. mutans* suspension after co-culturing with ZIF-8@PDA NP solution with different pH values (pH = 5.5, 6.0, 6.5, and 7.0) for 6 h. Data are presented as mean ± standard deviation with $n = 3$. $^*p < 0.05$, $^{**}p < 0.01$ and $^{***}p < 0.001$.

eradicate the biofilm. Furthermore, we assessed the number of regrown bacteria from the biofilms after various treatments (Fig. 5d and e). The bacteria incubated with ZIF-8@PDA NPs showed a 3-log CFU reduction (Fig. 5e), indicating that the combination of ZIF-8@PDA NPs and NIR effectively killed the bacteria within the biofilm, thereby preventing biofilm recolonization to a significant extent. Crystal violet (CV) staining was used to further quantify the residual amount of the biofilm after different treatments. We observed that the residual amount of the biofilm was minimal in the presence of ZIF-8@PDA NPs under NIR irradiation (Fig. 5f and g). These results confirmed that ZIF-8@PDA NPs could effectively eradicate the biofilm composed of *S. mutans* under NIR irradiation.

Furthermore, we studied the effect of ZIF-8@PDA NPs on the pH variation within the biofilm. To achieve this, we used enamel slices to simulate the tooth surface. Enamel slices covered with oral biofilms were immersed in ZIF-8@PDA NP suspension, PBS solution, and saliva solution for 30 min, and the pH values of the enamel slice surfaces were subsequently measured. Fig. S4 (ESI†) shows that the pH on the tooth surface consistently remained above 7 after immersion in the ZIF-8@PDA NP suspension, whereas the pH after immersion in PBS and artificial saliva was about 5, indicating a weakly acidic condition. These experiments demonstrated that ZIF-8@PDA NPs could effectively respond to and neutralize the acidic microenvironment of the pathological biofilm.

Based on the above results, we proposed a mechanism for the eradication of oral biofilms using ZIF-8@PDA NPs under NIR irradiation. It is well-established that the PDA coating exhibits exceptional interfacial adhesion properties, enabling it to readily bond to the biofilm surface upon initial contact.[57] Subsequently, the ZIF-8@PDA NPs respond to the acidic microenvironment of the biofilm (Fig. 4c), leading to the dissociation of the internal ZIF-8 NP structure and the release of Zn^{2+} ions. Zn^{2+} ions are known to have antimicrobial properties by disrupting bacterial cell membranes and interfering with essential enzymatic activities.[57] Meanwhile, under NIR irradiation, the ZIF-8@PDA NPs induce a photothermal effect, which causes local hyperthermia. PDA exhibits excellent adhesion, multifunctionality, and antibacterial properties.[57] It can generate

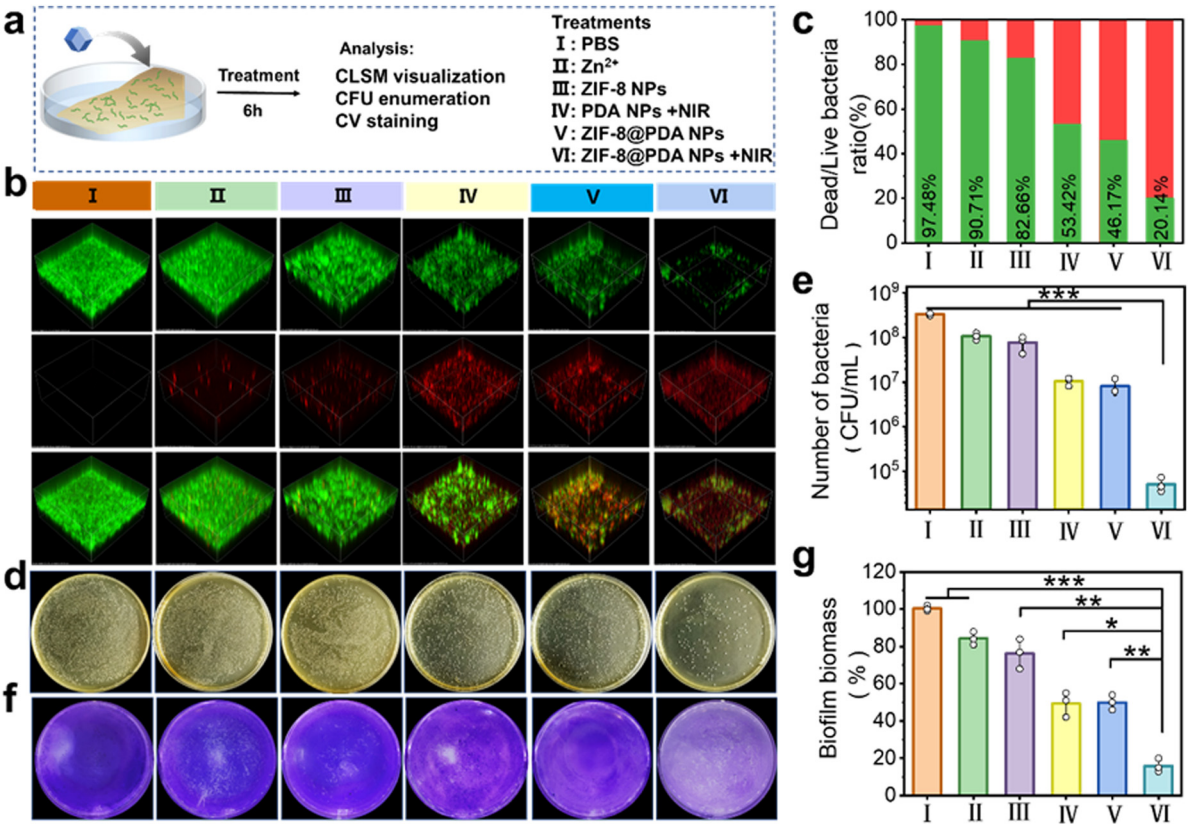

Fig. 5 Eradication of the mature biofilms *in vitro*. (a) Workflow illustrating the design and processing of experiments for biofilm eradication *in vitro*. (b) 3D reconstructed confocal images of *S. mutans* biofilms after co-culture with (I) the control (PBS solution), (II) $Zn(OAc)_2{\cdot}2H_2O$ solution, (III) ZIF-8 NP solution, (IV) PDA NP solution under an 808 nm laser, (V) ZIF-8@PDA NP solution and (VI) ZIF-8@PDA NP solution under an 808 nm laser. (c) The ratio of dead to live bacteria in mature biofilms after different treatments. (d) Representative photographs of biofilm colonies formed on BHI agar plates after different treatments. (e) CFU enumeration of mature biofilms after different treatments. (f) Crystal violet (CV) stained photographs of biofilms formed in pore plates after different treatments. (g) Percentages of residual biofilms after different treatments. Data are presented as mean ± standard deviation with $n = 3$. *$p < 0.05$, **$p < 0.01$ and ***$p < 0.001$.

nitro phenolic compounds through oxidative reactions, which subsequently react with amino groups on bacterial surfaces to form adhesive structures, thereby achieving antibacterial effects.[57] This not only induces the denaturation of bacterial DNA and proteins but also enhances the permeability of Zn^{2+} within the biofilm due to the increased diffusion coefficient.[58,59] In addition, hyperthermia has the potential to damage the biofilm, further accelerating the permeation of Zn^{2+} ions. Moreover, PDA has been shown to have excellent adhesion, multifunctionality, and antibacterial properties.[60,61] It can generate nitro phenolic compounds through oxidative reactions, which subsequently react with amino groups on bacterial surfaces, causing bacterial death. Thus, by synergizing the photothermal and antibacterial properties of Zn^{2+} ions, the antibacterial efficacy of each can be significantly enhanced. As treatment progresses, the destruction of bacteria and the eradication of the biofilm prevent the production of acidic substances from bacterial metabolism, thereby maintaining a stable pH level (Fig. 4e).

2.5. Biofilm eradication on the extracted teeth surface

To further explore the efficacy of ZIF-8@PDA NPs combined with NIR irradiation in biofilm removal on the surface of the extracted tooth, an *ex vivo* biofilm model was constructed using human teeth. The teeth were subjected to different treatments (Fig. 6a). Note that all treatments described in this section were exposed to an 808 nm laser (1.5 W cm^{-2}, 10 min). The results indicated that the temperature of teeth coated with ZIF-8@PDA NPs rapidly increased to 50 °C, respectively (Fig. 6b and c). Subsequently, the viable bacteria count in the biofilm was quantified using the plate count method (Fig. 6d). The results revealed that treatments involving Zn^{2+} + NIR had little effect on reducing the counts of *S. mutans* within the biofilm. Conversely, treatments with ZIF-8 NPs + NIR and PDA NPs + NIR were effective in decreasing bacterial counts. Notably, the ZIF-8@PDA NPs + NIR treatment showed the most promising results, decreasing bacterial counts by 3-log CFU units (Fig. 6e). This result was consistent with the *in vitro* biofilm eradication experiments (Fig. 5e).

The morphology of biofilms on tooth surfaces after different treatments was examined using SEM. As shown in Fig. 6f, the biofilm of *S. mutans* completely covered the tooth surface when treated with PBS or Zn^{2+}, indicating that Zn^{2+} alone cannot eradicate the biofilm. After treatment with ZIF-8 NPs, the number of bacteria observed within the biofilm was notably

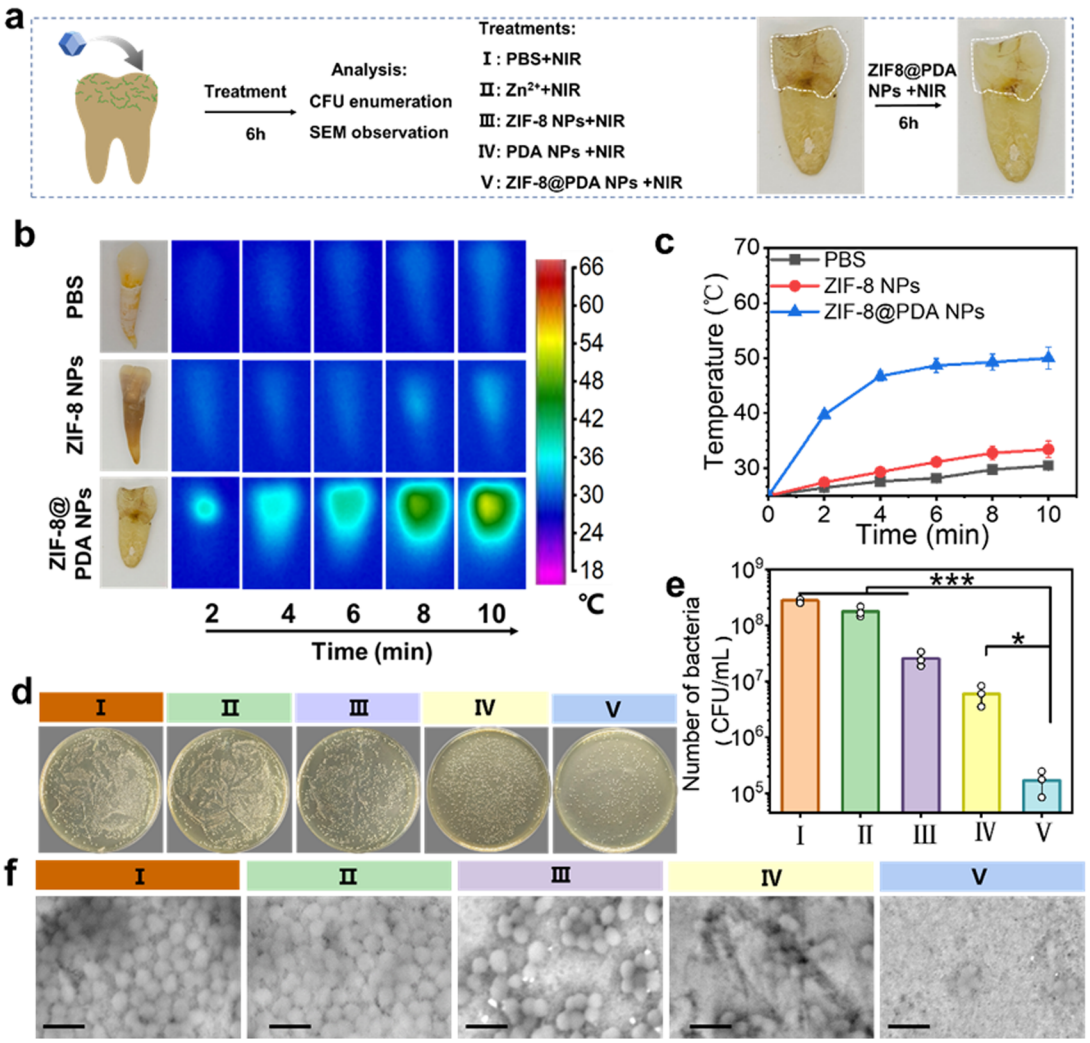

Fig. 6 *Ex vivo* eradication of mature biofilms on the teeth surface. (a) Workflow of the *ex vivo* biofilm eradication experiment and photographs of teeth treated with ZIF-8@PDA NPs under 808 nm laser at 1.5 W cm^{-2} for 10 min. (b) Infrared thermal photographs of teeth surfaces dipped in PBS solution and solutions containing ZIF-8 NPs and ZIF-8@PDA NPs under 808 nm laser at 1.5 W cm^{-2} for 10 min. (c) Temperature *versus* time curves for teeth surfaces subjected to different treatments. (d) Photographs and (e) CFU enumeration of bacteria cultured from biofilms that were scraped off the teeth after different treatments. (f) Representative SEM images of mature biofilms on tooth surfaces after different treatments, the scale bars represent 2 μm. Data are presented as mean ± standard deviation with $n = 3$. *$p < 0.05$, **$p < 0.01$ and ***$p < 0.001$.

decreased. Interestingly, treating with PDA NPs led to the disruption of the biofilm, confirming that photo-induced hyperthermia could damage the biofilm.[62] The ZIF-8@PDA NPs + NIR treatments almost eliminated the biofilm and the bacteria it harbored. We did not observe any well-formed dead bacteria, only some suspected debris (Fig. 6f). This result demonstrated the superior efficacy of the ZIF-8@PDA NPs + NIR in biofilm eradication.

2.6. Efficacy of ZIF-8@PDA NPs for oral biofilm eradication *in vivo*

To validate the efficacy of the ZIF-8@PDA NPs combined with NIR in removing oral biofilms *in vivo*, we established a rodent model infected with *S. mutans* (Fig. 7a). This is due to the progression of dental caries in rats is similar to that observed in humans, advancing from shallow caries to moderate caries and ultimately to deep caries with extensive lesions.[54] Sprague–Dawley (SD) rats were treated with PBS, ZIF-8 NPs + NIR, PDA NPs + NIR, ZIF-8@PDA NPs, and ZIF-8@PDA NPs + NIR. *In vivo* NIR imaging of SD rats showed that the temperature of teeth coated with ZIF-8 NPs, PDA NPs, and ZIF-8@PDA NPs rapidly increased, particularly in the ZIF-8@PDA NPs group, which reached up to 55 °C (Fig. 7b and c), which was high enough to eliminate oral bacteria. Throughout the treatment period, all groups of rats maintained good health status, with no significant difference in the body weight gain (Fig. 7d). Optical photographs of rat teeth observed after 7 days of treatment revealed that the bacterial biofilm on the rat teeth surfaces was significantly reduced following the ZIF-8@PDA NPs + NIR treatment. The degree of tooth whiteness was markedly superior compared to that of other treatment modalities (Fig. 7e).

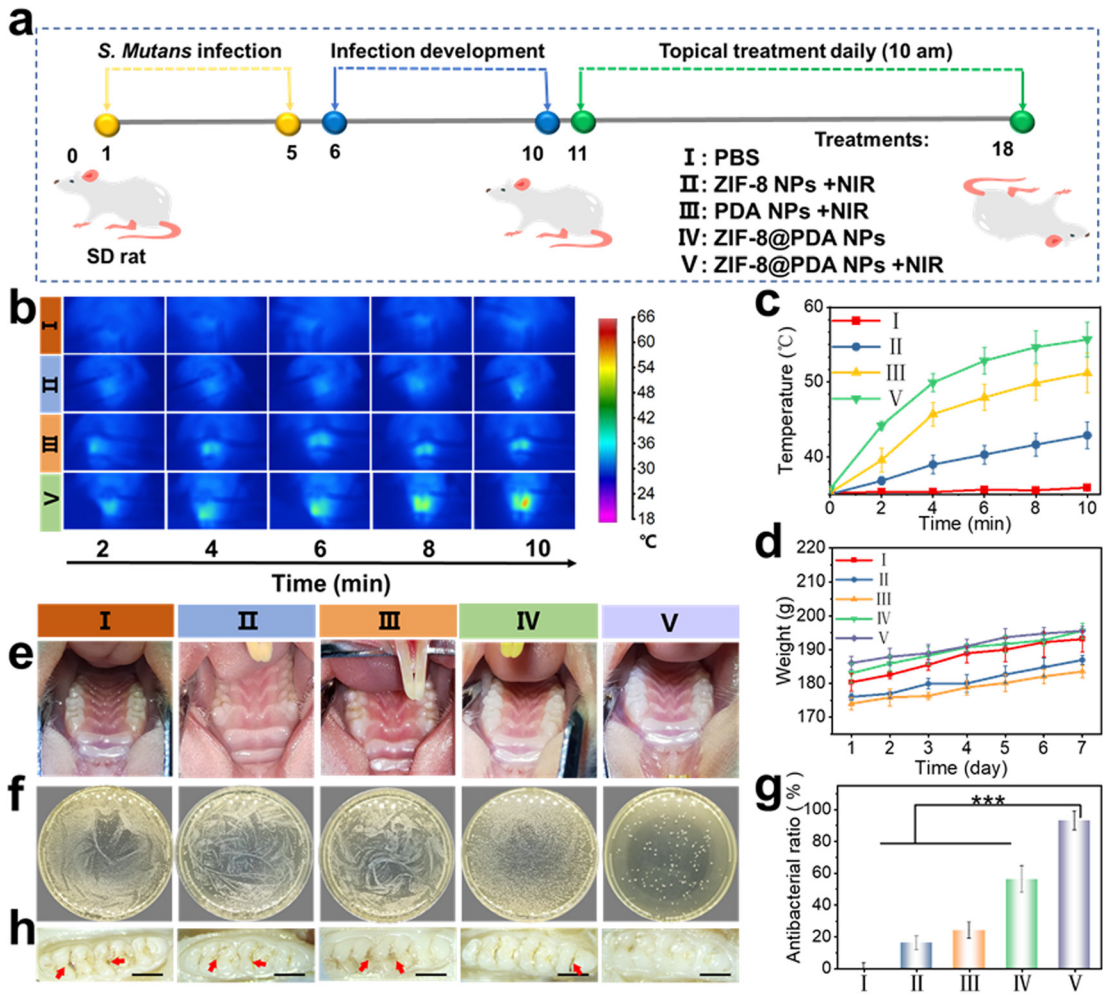

Fig. 7 Efficacy of ZIF-8@PDA NPs *in vivo*. (a) Design and treatment protocol for a rodent dental biofilm model. (b) *In vivo* body of NIR imaging from SD rats after treatment with ZIF-8 NPs, PDA NPs, and ZIF-8@PDA NPs under an 808 nm laser (1.5 W cm^{-2}, 10 min). (c) Temperature *versus* time curves of SD rats' teeth treatment with ZIF-8 NPs, PDA NPs, and ZIF-8@PDA NPs under an 808 nm laser (1.5 W cm^{-2}, 10 min) *in vivo*. (d) Monitoring of rat body weight during treatment. (e) Photographs of rodent dental biofilm models subjected to different treatments over 7 days. (f) Representative photographs of live dental bacterial colonies on BHI agar plates from rats in different groups after 7 days of treatment. (g) The antibacterial rate denotes one minus the ratio of the cultured bacterial count on rats' teeth after treatments different from those in the control group. (h) Representative photographs of rat teeth from different treatment groups after 7 days of treatment. The scale bars represent 2 mm. Data are presented as mean ± standard deviation with $n = 3$. $^{*}p < 0.05$, $^{**}p < 0.01$ and $^{***}p < 0.001$.

After 7 days of treatment, sterile swabs were used to collect oral microbiota for culturing bacteria on BHI agar plates. We defined the antibacterial rate as one minus the ratio of the cultured bacterial count on rats' teeth after different treatments to that in the control group (Fig. 7f and g). Treatments involving ZIF-8 NPs combined with NIR and PDA NPs combined with NIR did not achieve the desired ideal caries prevention effect. In contrast, treatment with ZIF-8@PDA NPs notably reduced the bacterial count; however, a significant number of viable bacteria persisted. Notably, when ZIF-8@PDA NPs were combined with NIR irradiation, the antibacterial rate reached 93 ± 5%, indicating superior antibacterial efficacy. Photographs of rat teeth were further examined to evaluate the therapeutic effects of different treatments (Fig. 7h). In the control group, ZIF-8 NPs + NIR group and PDA NPs + NIR group, lesions and caries were readily observable. The ZIF-8@PDA NP treatment showed a certain degree of therapeutic effect; however, localized remnants of the biofilm persisted. The ZIF-8@PDA NPs + NIR group exhibited the most remarkable therapeutic effect, significantly diminishing dental lesions and caries from the tooth surface. The treatment of ZIF-8@PDA NPs combined with NIR enhances the eradication of bacterial biofilms through the synergistic effect of Zn^{2+} release and photothermal therapy. Compared to traditional 1% sodium hypochlorite (NaOCl) irrigation and the single use of photothermal therapy, photodynamic therapy, Zn-MOF (Table S1, ESI†), the ZIF-8@PDA NPs combined with NIR method exhibits superior biocompatibility and a controlled release mechanism, thereby minimizing damage to healthy tissues and enhancing treatment safety. Furthermore, the gentle photothermal effect obviates the need for invasive procedures such as sandblasting and rubber cup polishing, markedly improving patient comfort and broadening its clinical applicability.

2.7. Biocompatibility assessment

The findings above demonstrated the effective eradication of oral bacteria and the efficient eradication of oral biofilms using the ZIF-8@PDA NPs + NIR treatments. Finally, we assessed the biocompatibility of ZIF-8@PDA NPs + NIR treatments through hemolysis and cell toxicity experiments. First, L929 cells were chosen to assess cytotoxicity. The live/dead cell staining revealed that ZIF-8@PDA NPs did not noticeably affect the morphology of L929 cells (Fig. 8a). Cell viability was further evaluated using the CCK-8 assay (Fig. 8b). The data revealed showed that, when the NP concentrations were below 200 μg mL^{-1}, cell viability remained above 90% in all groups: ZIF-8 NPs, ZIF-8@PDA NPs, and ZIF-8@PDA NPs + NIR. However, as the NP concentration increased, a decline in cell viability was observed in both the ZIF-8 NPs and ZIF-8@PDA NPs + NIR groups. Consequently, within a concentration of 200 μg mL^{-1}, the NPs demonstrated superior biocompatibility, and thus, the concentration of 200 μg mL^{-1} was employed for subsequent measurements. Furthermore, F-actin staining was performed to analyze the impact of ZIF-8@PDA NPs and ZIF-8@PDA NPs + NIR treatments on cell morphology and cytoskeleton (Fig. 8d). Both the ZIF-8@PDA NPs and the ZIF-8@PDA NPs + NIR treatments had a minimal impact on the structural organization of F-actin. It is noteworthy that the structural organization of F-actin was preserved even after NIR irradiation (Fig. 8d). In addition, a hemolysis assay was performed to assess the hemolytic potential of ZIF-8@PDA NPs on erythrocytes (Fig. 8c). When erythrocytes derived from fresh mouse blood cells were incubated in ultrapure water, they burst and released hemoglobin due to the low osmotic pressure of water. In contrast, the hemolysis rates for the pure PBS solution, as well as for the solutions containing the ZIF-8@PDA NPs (with or without NIR irradiation) were all below 5%, indicating excellent hemocompatibility.

To further investigate the *in vivo* biocompatibility and safety of the ZIF-8@PDA NPs and the ZIF-8@PDA NPs + NIR treatments, histological analysis using H&E staining was conducted on key organs, including the lip, tongue, and gingival tissue (Fig. S5 and S6, ESI†). Pathological image analysis revealed that following ZIF-8@PDA NPs and ZIF-8@PDA NPs + NIR treatments, no significant signs of adverse reactions were observed in any treatment group, including inflammatory responses, proliferative changes, tissue damage, or necrosis. Taken together,

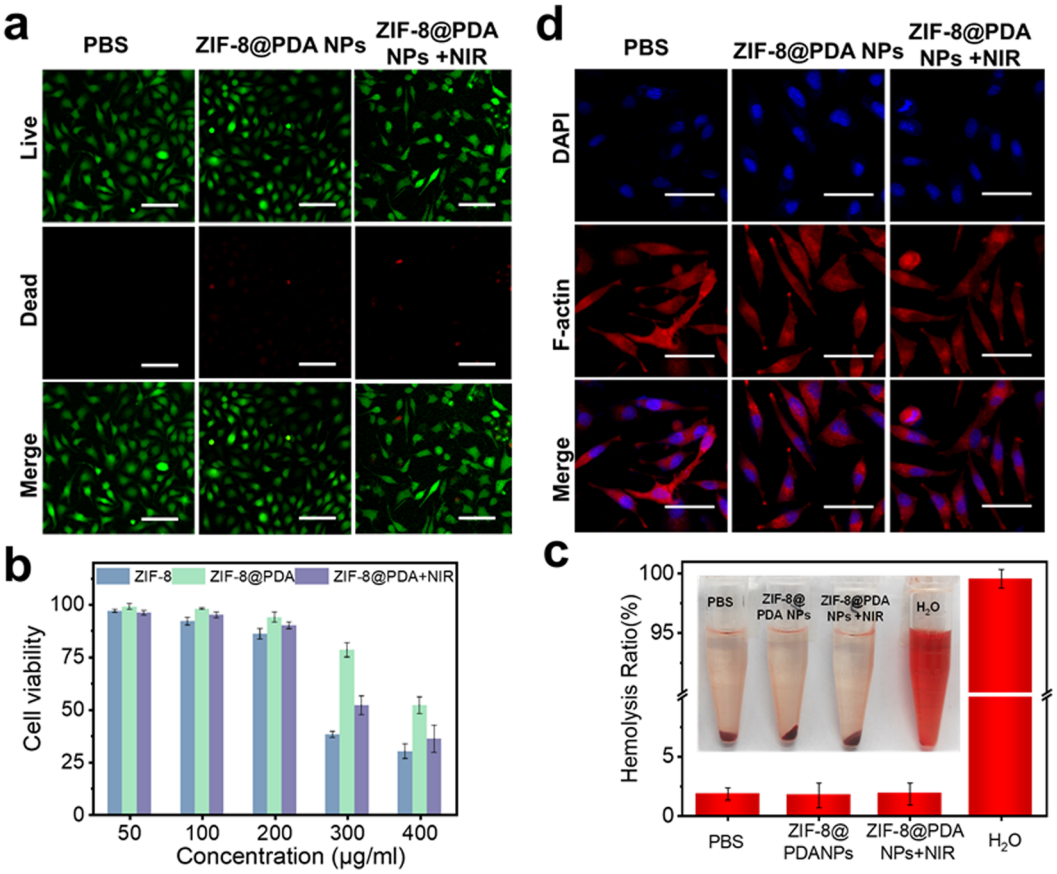

Fig. 8 Biocompatibility of ZIF-8@PDA NPs. (a) Fluorescence images of L929 cell viability/death staining after different treatments. The scale bar represents 100 μm. Dead cells are red; living cells are green. (b) Cell viability after different treatments using the CCK-8 assay. (c) Hemolysis ratio under different treatments co-incubated with blood cells for 1 h at 37 °C. The inset illustrates the corresponding photographs. (d) Fluorescence images of L929 cell F-actin staining under different treatment conditions. The scale bar represents 50 μm. F-actin is red; the nucleus is blue. Data are presented as means ± SD (n = 3).

these results showed the excellent biocompatibility of ZIF-8@PDA NPs and the biosafety of therapy using them.

3. Conclusions

In conclusion, we have developed ZIF-8@PDA NPs that degrade under mildly acidic conditions to release Zn^{2+} and convert light energy into heat, inducing localized hyperthermia. Using ZIF-8@PDA NPs enables a synergistic combination of photothermal and antibacterial metal ion therapy for effective oral biofilm eradication. This is because local hyperthermia could damage the biofilm, thereby accelerating the permeation of Zn^{2+} through it. Thus, by synergizing the photothermal and antibacterial properties of Zn^{2+} ions, the antibacterial efficacy of each can be significantly enhanced. Our results demonstrated that the therapy employing ZIF-8@PDA NPs, when subjected to NIR, exhibits remarkable antibacterial properties and proves effective in eradicating oral biofilms both *in vitro* and *ex vivo*. Furthermore, we used an *in vivo* rodent tooth biofilm model to demonstrate the suppression of dental caries. We also conducted a thorough study and confirmed that the NPs and the therapy using them are biocompatible. Beyond their application in clinical biofilm treatment, we anticipate that these NPs may be incorporated into toothpaste and utilized with near-infrared light-emitting toothbrushes. Their ease of synthesis, biocompatibility, affordability, and efficacy in eradicating biofilms could elevate conventional oral care practices.

4. Experimental section

4.1. Materials

Zinc acetate dihydrate ($Zn(OAc)_2{\cdot}2H_2O$), 2-methylimidazole (HmIm), glutaraldehyde, and dopamine hydrochloride (DA) were purchased from Aladdin Industrial Co., Ltd (China). Tris powder was acquired from Bio Basic Inc. (Canada). Polyglutamic acid was acquired from Xuankai Biological Technology (Nanjing) Co., Ltd (China). The CCK-8 assay kit was obtained from Beijing Labgic Technology Co., Ltd (China). The Live/Dead BacLight Bacterial Viability Kit (including SYTO9 and propidium iodide) and Calcein-AM/PI Cell Viability/Cytotoxicity Assay Kit were purchased from Beijing Beyotime Technology Co., Ltd (China). RhB-phalloidin (phalloidin labeled with RhB) and DAPI were obtained from Solarbio Life Sciences (China). *Streptococcus mutans* (*S. mutans*) and the murine gingival fibroblast cell (L929) were purchased from the American Type Culture Collection (USA). Dulbecco's modified Eagle's medium (DMEM) was supplied by VivaCell (China). The glass-bottom Petri dishes used for confocal fluorescence imaging were acquired from NEST Biotechnology (China).

4.2. Synthesis of ZIF-8 NPs and ZIF-8@PDA NPs

First, $Zn(OAc)_2{\cdot}2H_2O$ (0.219 g) and HmIm (1.6440 g) were dissolved in 4.5 mL ultrapure water, stirred thoroughly, and left for 24 h. Next, the white precipitate particles were washed with ultrapure water and dried at 50 °C to obtain ZIF-8 NPs. Then, the prepared ZIF-8 NPs (100 mg) were dispersed in Tris–HCl buffer solution (120 mL, pH = 8.5), followed by the slow addition of a certain amount of DA, and the proportions between ZIF-8 and PDA were 5 : 2, 1 : 1, and 2 : 5, respectively. The progress of the reaction is monitored by observing the color change from light white to dark brown. Afterward, ZIF-8@PDA NPs were collected through centrifugation (10 000 rpm), washing, and lyophilization. DA (40 mg) was dispersed in Tris–HCl buffer solution (120 mL, pH = 8.5) and stirred for 2 h to obtain PDA NPs.

4.3. The photothermal effect and pH sensitivity of ZIF-8@PDA NPs

The PBS, the ZIF-8 suspensions (200 μg mL^{-1}), and the ZIF-8@PDA NP suspensions with different concentrations (50, 100, 200, and 400 μg mL^{-1}) were placed in a centrifuge tube. Each sample was then irradiated with an 808 nm laser at a density of 1.5 W cm^{-2} for 10 min, respectively, and their real-time temperature changes were assessed using an infrared thermal imager (TiS40, Fluke, USA). The photothermal stability of ZIF-8@PDA NPs was evaluated by measuring the temperature changes over six cycles of laser on/off. The following equation can be used to calculate the photothermal conversion efficiency of ZIF-8@PDA NPs:

$$\eta = \frac{hA\left(\Delta T_{\max,\min} - \Delta T_{\max,H_2O}\right)}{I\left(1 - 10^{-A_\lambda}\right)}$$

where h represents the heat transfer coefficient, A is the surface area of the container, I means the laser power, A_λ represents the absorbance of ZIF-8@PDA NPs at 808 nm, and $\Delta T_{\max,\min}$ and $\Delta T_{\max,H_2O}$ stand for the temperature change of the ZIF-8@PDA NP dispersion and water at the maximum steady-state temperature, respectively.

To verify the photothermal effect of ZIF-8@PDA NPs on the tooth surface, PBS, the ZIF-8 NP suspension (200 μg mL^{-1}), and the ZIF-8@PDA NP suspension (200 μg mL^{-1}) were each applied to the extracted human teeth using an applicator. The teeth were then exposed to NIR for 10 min. The real-time temperature of the teeth was recorded using an infrared thermal imager. ZIF-8@PDA NPs were added into PBS solutions with different pH values (pH = 5.5, 6.0, 6.5, and 7.0), and incubated at 37 °C for 2, 4, 6, and 8 h. Following incubation, the samples underwent centrifugation at 10 000 rpm, enabling the collection of solid residues. These residues were subsequently weighed and used for quantitative calculations of the hydrolysis rate of ZIF-8@PDA NPs. Additionally, the morphological alterations of the ZIF-8@PDA NPs in solutions with different pH values and incubated at 37 °C for 2 h were examined by SEM.

4.4. Antibacterial activity and biofilm eradication *in vitro*

To investigate the oral antibacterial efficacy of ZIF-8@PDA NPs with NIR laser, *Streptococcus mutans* (*S. mutans*) was chosen for the antibacterial assays. To assess the biofilm eradication efficacy of synergistic photothermal and antibacterial metal ion therapy, a mature oral biofilm was established using

S. mutans in vitro. Further details about these experimental methods are detailed in the ESI.†

4.5. Establishment and treatment of a mature biofilm model on extracted teeth *ex vivo*

To further investigate the biofilm removal efficacy of ZIF-8@PDA NPs plus NIR irradiation, we established an oral biofilm model *ex vivo* to assess whether various treatments effectively eliminated mature biofilms on extracted tooth surfaces. The human teeth were provided by the Stomatological Hospital of Jilin University. The extracted human teeth enamels were washed several times with sterile PBS which was cut into slices (4 mm × 4 mm) and immersed in the *S. mutans* suspension (1×10^8 CFU mL^{-1}) for 24 h. Then, the extracted slices were washed 3 times with PBS and added BHI medium containing: (I) the control (PBS solution), (II) 20 μg mL^{-1} $Zn(OAc)_2{\cdot}2H_2O$, (III) 200 μg mL^{-1} ZIF-8 NPs, (IV) 200 μg mL^{-1} PDA NPs and (V) 200 μg mL^{-1} ZIF-8@PDA NPs. All the solutions contained 1% polyglutamic acid to increase the adhesion of the NPs to the extract teeth. After application, all slices were exposed to an 808 nm laser (1.5 W cm^{-2}, 10 min). Then, the extracted slices were co-cultured with various BHI media for 6 h in a 37 °C incubator. Subsequently, biofilms on the enamel surface were collected into PBS through vigorous agitation and then diluted. The bacterial suspensions were spread on an agar plate and incubated at 37 °C for 24 h to count the number of CFUs. Additionally, the biofilms on the enamel surface were observed using a SEM. Finally, the biofilms on the enamel surface were immersed in PBS, artificial saliva, or ZIF-8@PDA NP solutions for 30 min, respectively, and the pH of the enamel slices was measured.

4.6. Biosafety experiment

To assess the cytotoxicity of ZIF-8@PDA NPs, the survival rates of L929 mouse gingival fibroblast cells treated with ZIF-8 NPs, ZIF-8@PDA NPs and ZIF-8@PDA NPs + NIR were measured at 24 h using the CCK-8 assay. The NP concentrations used were 50, 100, 200, 300, and 400 μg mL^{-1}, respectively, and the NIR light was obtained from an 808 nm laser at a density of 1.5 W cm^{-2} for 10 min. Then, the cells treated with PBS, ZIF-8@PDA NPs (200 μg mL^{-1}) and ZIF-8@PDA NPs + NIR were stained with a Calcein-AM/PI assay kit for both living and dead cells and observed by CLSM fluorescence imaging.[63] After that, the cell nuclei and cytoskeleton were stained using RhB-phalloidin and DAPI and observed by confocal laser scanning microscopy (CLSM) fluorescence imaging.[64,65] Additionally, the hemolysis rates were determined through a hemolysis assay of different treatments. Finally, histological evaluation was performed to assess the toxicity of the nanomaterials *in vivo*. Further details about these experimental methods are detailed in the ESI.†

4.7. *In vivo* therapeutic effect

All animal experiments conformed to the guidelines established by the Animal Care and Ethics Committee of the Changchun Institute of Applied Chemistry (CIAC), Chinese Academy of Sciences. The occurrence of lesions on rat teeth' smooth surface and fissure surface was measured using a stereomicroscope (NSZ-405, China) to assess the therapeutic effects of PBS, ZIF-8 NPs + NIR, PDA NPs + NIR, ZIF-8@PDA NPs, and ZIF-8@PDA NPs + NIR treatments for the oral biofilm *in vivo*. The coating of nanoparticles was performed by dipping a cotton swab into the solution and then applying it to the surface of the teeth. NIR was applied twice a day at a density of 1.5 W cm^{-2} for 10 minutes each time, and the real-time temperature changes were monitored using an infrared thermal imager. A standard plate counting assay was conducted to evaluate the antibacterial effect. The hearts, livers, spleens, lungs, kidneys, tongue mucosa, lips, and gingival tissues of rats were collected for H&E staining Further details about these experimental methods are detailed in the ESI.†

Author contributions

Ge Pan: conceptualization, methodology, investigation, validation, and writing – original draft preparation. Miaomiao Zhang: data curation, formal analysis, investigation, and writing – review. Jinyao Zheng and Zongjia Li: methodology. Qian Duan: conceptualization, writing – review and editing, and funding acquisition. Dapeng Wang: conceptualization, funding acquisition, investigation, methodology, project administration, resources, supervision, validation, and writing – review and editing.

Data availability

All relevant data are within the manuscript and its additional files.

Conflicts of interest

The authors declare no conflict of interest.

Acknowledgements

This work was supported by the National Key Research and Development Program of China (Grant No. 2021YFC2101700), the Natural Science Foundation of Jilin Province (Grant No. 20240101179JC), the Key Research Program of Frontier Sciences, Chinese Academy of Sciences (Grant No. ZDBS-LY-SLH033) and the Special Project for High-tech Industrialization of Science and Technology Cooperation between Jilin Province and Chinese Academy of Sciences (Grant No. 2023SYHZ0030).

References

1 L. Sedghi, V. DiMassa, A. Harrington, S. V. Lynch and Y. L. Kapila, *Periodontol. 2000*, 2021, **87**, 107–131.
2 H.-C. Flemming, J. Wingender, U. Szewzyk, P. Steinberg, S. A. Rice and S. Kjelleberg, *Nat. Rev. Microbiol.*, 2016, **14**, 563–575.

3 L. Gao, T. Xu, G. Huang, S. Jiang, Y. Gu and F. Chen, *Protein Cell*, 2018, **9**, 488–500.
4 H. C. Flemming and J. Wingender, *Nat. Rev. Microbiol.*, 2010, **8**, 623–633.
5 J. L. Baker, J. L. M. Welch, K. M. Kauffman, J. S. McLean and X. S. He, *Nat. Rev. Microbiol.*, 2024, **22**, 89–104.
6 D. Davies, *Nat. Rev. Drug Discovery*, 2003, **2**, 114–122.
7 D. S. W. Benoit, K. R. Sims, Jr. and D. Fraser, *ACS Nano*, 2019, **13**, 4869–4875.
8 Z. Yin, Y. Liu, A. Anniwaer, Y. You, J. Guo, Y. Tang, L. Fu, L. Yi and C. Huang, *Adv. Mater.*, 2023, 2305633.
9 Y. Yu, Y. Cheng, L. Tan, X. Liu, Z. Li, Y. Zheng, T. Wu, Y. Liang, Z. Cui, S. Zhu and S. Wu, *Chem. Eng. J.*, 2022, **431**, 133279.
10 P. S. Stewart and J. William Costerton, *Lancet*, 2001, **358**, 135–138.
11 Y. Tang, Q.-X. Huang, D.-W. Zheng, Y. Chen, L. Ma, C. Huang and X.-Z. Zhang, *Mater. Today*, 2022, **53**, 71–83.
12 H. Koo, R. N. Allan, R. P. Howlin, P. Stoodley and L. Hall-Stoodley, *Nat. Rev. Microbiol.*, 2017, **15**, 740–755.
13 S. E. Birk, J. A. J. Haagensen, H. K. Johansen, S. Molin, L. H. Nielsen and A. Boisen, *Adv. Healthcare Mater.*, 2020, **9**, 1901779.
14 Y. Yang, Y. Qian, M. Zhang, S. Hao, H. Wang, Y. Fan, R. Liu, D. Xu and F. Wang, *J. Mater. Sci. Technol.*, 2023, **133**, 77–88.
15 Y. Liu, L. Shi, L. Su, H. C. van der Mei, P. C. Jutte, Y. Ren and H. J. Busscher, *Chem. Soc. Rev.*, 2019, **48**, 428–446.
16 S. Wu, C. Xu, Y. Zhu, L. Zheng, L. Zhang, Y. Hu, B. Yu, Y. Wang and F.-J. Xu, *Adv. Funct. Mater.*, 2021, **31**, 2103591.
17 Y. Li, Y. Liu, Y. Ren, L. Su, A. Li, Y. An, V. Rotello, Z. Zhang, Y. Wang, Y. Liu, S. Liu, J. Liu, J. D. Laman, L. Shi, H. C. van der Mei and H. J. Busscher, *Adv. Funct. Mater.*, 2020, **30**, 2004942.
18 Y. Yang, M. Li, G. Pan, J. Chen and B. Guo, *Adv. Funct. Mater.*, 2023, **33**, 2214089.
19 Y. Yang, X. Wu, C. He, J. Huang, S. Yin, M. Zhou, L. Ma, W. Zhao, L. Qiu, C. Cheng and C. Zhao, *ACS Appl. Mater. Interfaces*, 2020, **12**, 13698–13708.
20 X. Liu, X. Sun, Y. Peng, Y. Wang, D. Xu, W. Chen, W. Wang, X. Yan and X. Ma, *ACS Nano*, 2022, **16**, 14666–14678.
21 J. Wang, S. P. Teong, S. N. Riduan, A. Armugam, H. Lu, S. Gao, Y. K. Yean, J. Y. Ying and Y. Zhang, *J. Am. Chem. Soc.*, 2024, **146**, 599–608.
22 R. Li, T. Chen and X. Pan, *ACS Nano*, 2021, **15**, 3808–3848.
23 A. Wang, G. Fan, H. Qi, H. Li, C. Pang, Z. Zhu, S. Ji, H. Liang, B. Jiang and X. Shen, *Biomaterials*, 2022, **289**, 121798.
24 F. Kunisch, C. Campobasso, J. Wagemans, S. Yildirim, B. K. Chan, C. Schaudinn, R. Lavigne, P. E. Turner, M. J. Raschke, A. Trampuz and M. Gonzalez Moreno, *Nat. Commun.*, 2024, **15**, 8572.
25 A. Wang, L. Li, L. Zheng, B. P. Jiang, Y. Liu, R. Huang, H. Qiu, S. Ji, H. Liang and X. C. Shen, *Aggregate*, 2024, e662.
26 G. M. Neelgund, A. Oki, S. Bandara and L. Carson, *J. Mater. Chem. B*, 2021, **9**, 1792–1803.
27 Z. Yuan, C. Lin, Y. He, B. Tao, M. Chen, J. Zhang, P. Liu and K. Cai, *ACS Nano*, 2020, **14**, 3546–3562.
28 W. Xiong, L. Wang, X. Chen, H. Tang, D. Cao, G. Zhang and W. Chen, *J. Mater. Chem. B*, 2020, **8**, 5234–5244.
29 T. C. Pagonis, J. Chen, C. R. Fontana, H. Devalapally, K. Ruggiero, X. Song, F. Foschi, J. Dunham, Z. Skobe, H. Yamazaki, R. Kent, A. C. R. Tanner, M. M. Amiji and N. S. Soukos, *J. Endod.*, 2010, **36**, 322–328.
30 M. Chen, J. Zhang, J. Qi, R. Dong, H. Liu, D. Wu, H. Shao and X. Jiang, *ACS Nano*, 2022, **16**, 7732–7744.
31 P. C. Naha, Y. Liu, G. Hwang, Y. Huang, S. Gubara, V. Jonnakuti, A. Simon-Soro, D. Kim, L. Gao, H. Koo and D. P. Cormode, *ACS Nano*, 2019, **13**, 4960–4971.
32 J. Xiao, L. Hai, Y. Li, H. Li, M. Gong, Z. Wang, Z. Tang, L. Deng and D. He, *Small*, 2022, **18**, 2105465.
33 Y. Mu, H.-H. Tran, Z. Xiang, A. Majumder, E. Hsu, E. Steager, H. Koo and D. Lee, *Small*, 2024, 2402292.
34 L. Chen, M. Peng, H. Li, J. Zhou, W. He, R. Hu, F. Ye, Y. Li, L. Shi and Y. Liu, *Adv. Mater.*, 2024, **36**, 2306376.
35 L. Xiao, M. Feng, C. Chen, Q. Xiao, Y. Cui and Y. Zhang, *Adv. Mater.*, 2023, 2304982.
36 Y. Yu, Y. Zhang, Y. Cheng, Y. Wang, Z. Chen, H. Sun, X. Wei, Z. Ma, J. Li, Y. Bai, Z. Wu and X. Zhang, *Bioact. Mater.*, 2022, **13**, 269–285.
37 J. Wang, B. Hao, K. Xue, H. Fu, M. Xiao, Y. Zhang, L. Shi and C. Zhu, *Adv. Mater.*, 2022, **34**, 2205653.
38 L. He, J. Dragavon, S. Cho, C. Mao, A. Yildirim, K. Ma, R. Chattaraj, A. P. Goodwin, W. Park and J. N. Cha, *J. Mater. Chem. B*, 2016, **4**, 4455–4461.
39 Y. Li, X. Liu, B. Li, Y. Zheng, Y. Han, D.-f Chen, K. W. K. Yeung, Z. Cui, Y. Liang, Z. Li, S. Zhu, X. Wang and S. Wu, *ACS Nano*, 2020, **14**, 8157–8170.
40 L. Wang, C. Zhang, J. Zhao, Z. Zhu, J. Wang, W. Fan and W. Jia, *Adv. Mater.*, 2024, **36**, 2308110.
41 W. Guo, Y. Wang, K. Zhang, X. Dai, Z. Qiao, Z. Liu, B. Yu, N. Zhao and F. Xu, *Chem. Mater.*, 2023, **35**, 6853–6864.
42 S. Gopalakrishnan, A. Gupta, J. M. V. Makabenta, J. Park, J. J. Amante, A. N. Chattopadhyay, D. Matuwana, C. J. Kearney and V. M. Rotello, *Adv. Healthcare Mater.*, 2022, **11**, 2201060.
43 C. Montoya, L. Roldan, M. Yu, S. Valliani, C. Ta, M. Yang and S. Orrego, *Bioact. Mater.*, 2023, **24**, 1–19.
44 S. Goel, C. A. Ferreira, F. Chen, P. A. Ellison, C. M. Siamof, T. E. Barnhart and W. Cai, *Adv. Mater.*, 2018, **30**, 1704367.
45 C. R. Mendes, G. Dilarri, C. F. Forsan, V. d M. R. Sapata, P. R. M. Lopes, P. B. de Moraes, R. N. Montagnolli, H. Ferreira and E. D. Bidoia, *Sci. Rep.*, 2022, **12**, 2658.
46 M. Taheri, D. Ashok, T. Sen, T. G. Enge, N. K. Verma, A. Tricoli, A. Lowe, D. R. Nisbet and T. Tsuzuki, *Chem. Eng. J.*, 2021, **413**, 127511.
47 Z. Lv, X. Zhang, Q. Gao, C. Wen, Y. He, H. Tan, L. Qian, W. Qi, X. Chen and Z. Li, *Adv. Funct. Mater.*, 2024, **34**, 2409274.
48 Y. Lu, D. Fan, Z. Shen, H. Zhang, H. Xu and X. Yang, *Nano Energy*, 2022, **95**, 107016.
49 Z. Wang, Y. Zou, Y. Li and Y. Cheng, *Small*, 2020, **16**, 1907042.
50 T. Wu, L. Huang, J. Sun, J. Sun, Q. Yan, B. Duan, L. Zhang and B. Shi, *Carbohydr. Polym.*, 2021, **269**, 118276.

51 M. Song, J. Xing, H. Cai, X. Gao, C. Li, C. Liu, X. Li, X. Fu, S. Ding, W. Cheng and R. Chen, *ACS Nano*, 2023, **17**, 10748–10759.
52 J. Ruan, H. Liu, B. Chen, F. Wang, W. Wang, Z. Zha, H. Qian, Z. Miao, J. Sun, T. Tian, Y. He and H. Wang, *ACS Nano*, 2021, **15**, 11428–11440.
53 L. Chen, M. Peng, J. Zhou, X. Hu, Y. Piao, H. Li, R. Hu, Y. Li, L. Shi and Y. Liu, *Adv. Mater.*, 2023, **35**, 2301664.
54 N. B. Pitts, D. T. Zero, P. D. Marsh, K. Ekstrand, J. A. Weintraub, F. Ramos-Gomez, J. Tagami, S. Twetman, G. Tsakos and A. Ismail, *Nat. Rev. Dis. Primers*, 2017, **3**, 17030.
55 G. Pan, H. Wang, Z. Li, J. Zheng, B. Peng, Q. Duan and M. Zhang, *Colloids Surf., B*, 2024, **243**, 114133.
56 Z. Li, W. Wei, M. Zhang, X. Guo, B. Zhang, D. Wang, X. Jiang, F. Liu and J. Tang, *Adv. Healthcare Mater.*, 2023, **12**, 2301060.
57 P. Yang, F. Zhu, Z. Zhang, Y. Cheng, Z. Wang and Y. Li, *Chem. Soc. Rev.*, 2021, **50**, 8319–8343.
58 K. Lyu, H. Chen, J. Gao, J. Jin, H. Shi, D. K. Schwartz and D. Wang, *Biomacromolecules*, 2022, **23**, 4709–4717.
59 K. Lyu, Y. Zhao, M. Zhang, J. Tang, J. Zhang, Y. Liu, X. Bian, X. Chen, H. Chen and D. Wang, *Langmuir*, 2023, **39**, 13534–13545.
60 D. Wang, H. Wu, L. Liu, J. Chen and D. K. Schwartz, *Phys. Rev. Lett.*, 2019, **123**, 118002.
61 M. Hu, H. Chen, H. Wang, S. Burov, E. Barkai and D. Wang, *ACS Nano*, 2023, **17**, 21708–21718.
62 C. Shuai, J. Zan, F. Deng, Y. Yang, S. Peng and Z. Zhao, *ACS Sustainable Chem. Eng.*, 2021, **9**, 1814–1825.
63 Z. Zhang, H. Chen, M. Hu and D. Wang, *J. Am. Chem. Soc.*, 2023, **145**, 10512–10521.
64 Y. Zhao, H. Chen, S. Geng, S. Liu and D. Wang, *Chin. J. Chem.*, 2023, **41**, 3245–3252.
65 H. Chen, M. Hu, Y. Zhao, K. Lyu, Y. Xu, Y. Sun, Z. Xie, J. Huang and D. Wang, *Aggregate*, 2024, **6**, e649.